# Supplementary Information

## S1 CGCNN-HD Model Performance

The CGCNN-HD is a variant of the CGCNN with a hyperbolic tangent function and an additional dropout layer as proposed by Noh *et al.* [1], shown in **Figure S1**. First, the hyperbolic tangent function stands to improve the model interpretability, and the dropout layer is used for the Bayesian approximation of the formation energy. Interestingly, the dropout operation can be understood as a Monte Carlo operation where, the connections between nodes in the full connected neural network (FCNN) are zeroed with a defined probability (p dropout), which means that for every iteration, different model architectures of the FCNN are trained. Consequently, the repeated prediction of a dropout model has considered Monte Carlo sampling being able to form a predictive distribution. As a result, the mean (μ) and variance ( ∫) correspond to the predicted property and its uncertainty. Note that, we have searched the dropout probability on a number of samples as hyperparameters in order to optimize its effect being characterized through uncertainty quantification approaches.

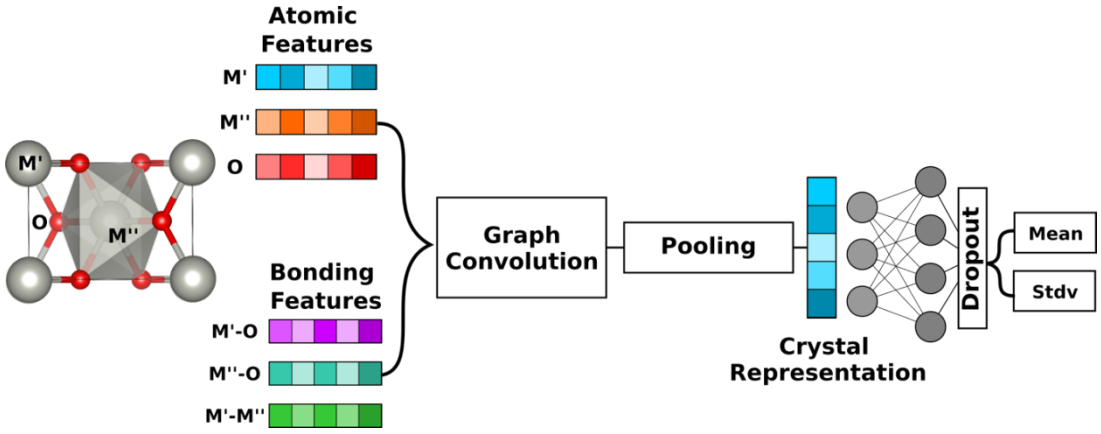


**Figure S1.** CGCNN-HD model architecture. [1]

The CGCNN-HD model hyperparameters were optimized using the Optuna package [2], where each search step was allowed to train for 100 epochs with a maximum number of exploration steps of 200, as shown in the following table.

**Table S1.** CGCNN-HD hyperparameters, definition, search range and optimized value.

| Hyperparameter | Definition | Range | Opt. Value |
|---|---|---|---|
| atom_fea_len | Hidden atoms features in conv. layer | 16-256 | 85 |
| h_fea_len | Hidden features after pooling | 16-256 | 160 |
| n_h | Hidden layers after pooling | 1-6 | 3 |
| n_conv | Convolutional layers | 1-8 | 5 |
| learning rate | Model's weight updating | $10^{-4}$-$10^{-2}$ | 0.0044 |
| optimizer | Optimization algorithm | Adam - SGD | Adam |
| p_dropout | Probability to be zeroed | 0.1-1.0 | 0.5 |
| sampling | To obtain a distribution | 50-1000 | 890 |

**Figure S2** consists of two general parts. Both parts contain a parity plot (left), calibration curve (middle), and predicted-uncertainty distribution (right) of our model on different unseen data: (1) Materials Project based test dataset (10% of the 36,465 metal oxide bulk structures) and (2) a random metal substitution on bimetallic oxides (2,000) dataset which was computed in our end. In this regard, the parity plot exhibits the accuracy of the model, the calibration curve shows the honesty of the model's uncertainty predictions, and the uncertainty distribution displays the sharpness of the model's uncertainty predictions.

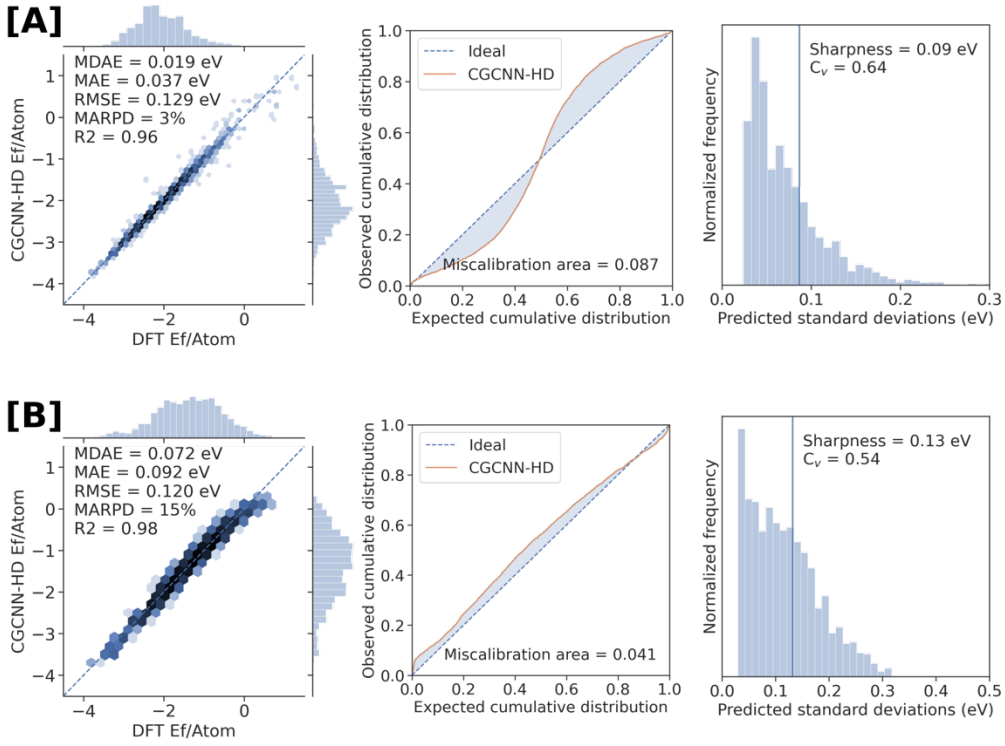


**Figure S2.** CGCNN-HD model performance as parity plot, calibration curve, and uncertainty distribution for (a) test dataset (10%) and (b) random metal substitutions dataset.

Regarding the parity plots (left), we can see that the trained model achieves a good accuracy on unseen bulk structures, even though they are no longer relaxed structures. Therefore, the MAE values are 0.032 and 0.092 eV/Atom for the Materials Project and for the random substituted testing datasets with a R score of 0.96 and 0.98, respectively. Moreover, compared to the MAE achieved by the original CGCNN-HD, which is reported to be 0.296 eV/Atom after applying the lattice scaling approach, states the good performances of the model obtained in the work. To the best of our knowledge, this difference mainly comes from the size of the training dataset.

The honesty of our model was estimated through the calibration curve plot (middle). A well-calibrated model has residuals that create Gaussian distributions whose standard deviations are close to the model's predicted standard deviation, thus approaching the ideal diagonal line. We quantified this closeness, so-called miscalibration area, as the area between the calibration

curve and the ideal diagonal. We found that our model, resolves on low miscalibration areas (0.087 and 0.041), although slightly underconfident on the 10 % of MP test set. Finally, sharp models have uncertainty distributions (Right) that tend to zero (0.09 and 0.13) and high coefficient of variation (C = 0.64 and 0.54). Note that sharpness should not be won at the cost of calibration.

# S2 DFT Method

All DFT periodic boundary calculations were performed with the spin-polarized formalism as implemented in the Vienna Ab-initio Simulation Package (VASP-6.2.1) [3,4] and using the GGA PBE functional. Ionic cores were described with the projector augmented wave pseudopotentials (PAW)[5] and the valence electrons were represented through a plane-wave basis set with a kinetic energy cut-off of 500 eV. A (50/a, 50/b, 50/c) and (30/a, 30/b, 1) $\wp$-centered Kpoint mesh[6] was employed to describe the first Brillouin zone for bulks and surfaces, respectively. The energy convergence criterion was fixed to 10 eV for the electronic structure, while the Hellman-Feynman forces criterion for geometry relaxation was set to smaller than 0.05 $eV$ Å$^{-1}$. All crystal structure manipulations and data analysis were carried out using the Python Materials Genomics package (Pymatgen) and Custodian library[7] as automatic error handlers.

The proposed equilibrium bulk structure for $RuTiO_4$, $RuCrO_4$, and $RuCrTiO_x$, and were obtained through atom substitution on a rutile structure template with ($P4_2/mnm$ $-136$) spacegroup retrieved from Materials Project [8] and computed through the equations of states (EOS). The EOS was performed by computing the energy of isotropic deformations through a linear strain that ranged from -5% to 5% of the optimized structure from each material. The above mentioned method was performed on different magnetic configurations, non-magnetic (NM), anti-ferromagnetic (AFM) and ferromagnetic (FM). To that end, the initial magnetic moments were derived using the Crystal Field Theory using the Voronoi algorithm to

determine the metal coordination number and the transition metal row for the low or high spin configuration, scaling the initial magnetic moments by 1.2. The Crystal Orbital Hamilton Population (COHP) analysis was used to quantify the bonding interactions and partition these interactions by specific ion-ion pairs within a range between 0.6 to 6.0 Å to quantify the percentage of covalency within each structure using the LOBSTER code. [9,10]

The main crystallographic orientations (110) and (101) were represented as non-dipolar and stoichiometric slab models, as experiments revealed as the most contributing ones to the nanoparticle shape. Slab models were built by considering a (2x2) supercell, cut from the equilibrium bulk structure. All slabs present a 4-layer thickness to ensure reasonable converged surface energy. The c value was set to 35 Å ensuring an interlayer distance of at least 21 Å to minimize the interaction between replicas at the (hkl) perpendicular direction. During optimizations, cell parameters were kept fixed, while the atoms positions were fully relaxed. Surface energy was computed with the following equation:

$$\gamma_{(hkl)} = \frac{E_{slab} - (N \cdot E_{bulk})}{2 \cdot A} \qquad (1)$$

Where $E_{slab}$ is the energy corresponding to the relaxed surface; $E_{bulk}$ is the fully relaxed oriented bulk energy; N is the number of formula units in the slab per unit in the bulk unit cell; and 2A is the corresponding two cross-section areas of the slab.

The coverage effects of reaction intermediates (OH*, O*) may significantly impact the local environment of the active site, resulting in changes in the adsorption strength of the OER reaction intermediates. Consequently, it is important to determine the most stable surface coverage at pH=0 and under typical applied potential ranges of OER (1.20 - 2.0 V vs SHE) to more reasonably describe the OER activity. Therefore, we modeled at three extreme coverages clean (*), OH*-covered, and O*-covered and the termination corresponding to most stable coverage at 1.6 V vs RHE was selected as the starting point for the reactivity calculations. In

total 50 DFT calculations were performed to generate the Surface Pourbaix diagrams for $RuTiO_4$, $RuCrO_4$, and $RuCrTiO_x$ and benchmarks $IrO_2$ and $RuO_2$.

OER catalytic activities of the different surface structures were determined by the theoretical overpotential ($\eta_{OER}$) and the potential-determining step (PDS) by assuming an associative reaction mechanism with O*, OH* and OOH* as reaction intermediates. The four proton-coupled electron transfers (PCET) reactions under acidic conditions are:

$$H_2O + (*) \rightarrow OH^* + (H^+ + e^-) \quad (2)$$

$$OH^* \rightarrow O^* + (H^+ + e^-) \quad (3)$$

$$O^* + H_2O \rightarrow OOH^*(H^+ + e^-) \quad (4)$$

$$OOH^* \rightarrow O_2 + (*) + (H^+ + e^-) \quad (5)$$

The computational hydrogen electrode (CHE) was used to express the chemical potential of the proton-electron pair $H^+ + e^-$ which is related to the chemical potential of based on the equilibrium $\mu[H^+] + \mu[e^-] = 0.5\ \mu\left[H_{2(g)}\right]$ at 0 $V_{RHE}$ and corrects the driving force with the deviation of the applied potential from the equilibrium situation. To avoid the use of electronic energy, which is difficult to determine correctly within standard GGA-DFT, the experimental free energy of $2H_2O \rightarrow O_2 + 2H_2 (\Delta G = 4.92eV)$ was used. [11–13] Therefore, the Gibbs free energies of reactions 2-5 depend on the adsorption free energies of the reaction intermediates ($\Delta G_{OH*}$ , $\Delta G_{O*}$, $and\ \Delta G_{OOH*}$) which are calculated relative to $H_2O$(g) and $H_2$(g) at U = 0 V and standard conditions. In total, 130 adsorption calculations were performed to calculate the adsorption free energies of the reaction intermediates, considering multiple orientations for OH* and OOH* on the surface termination for all the materials, and selecting the most stable one in each case.

The theoretical thermodynamic OER overpotential, which is a measure of the activity of a catalyst, is then defined from Gibbs free energies of reactions 2-5:

$$\eta_{OER}(V) = \frac{[\Delta G_{OH}, \Delta G_O - \Delta G_{OH}, \Delta G_{OOH} - \Delta G_O, 4.92 - \Delta G_{OOH}]}{e} - 1.23 \quad (6)$$

The step with the largest value in eq. 6 is referred to as the potential-determining step (PDS). It is important to note that the overpotential should not be compared directly with a measured overpotential since the measured overpotential depends on the current density.

**Table S2.** List of Ru-based rutile oxides that are generated stability screening using our CGCNN-HD model. The table is divided into two groups: green highlighted cells where $\Delta G_{pbx} < RuO_2$ (0.302 eV) and red highlighted cells where $\Delta G_{pbx} > RuO_2$. The green highlighted cells were sorted by the M-O covalency percentage.

| $M_1$ | $M_2$ | $\Delta G_{pbx}$ eV | Covalency % |
|---|---|---|---|
| **Ru** | **Ti** | **0.25** | **95.92** |
| Ru | Sn | 0.258 | 93.75 |
| Ru | Ge | 0.274 | 92.5 |
| Ru | Au | 0.213 | 91.3 |
| Ru | Ga | 0.269 | 88.87 |
| **Ru** | **Cr** | **0.253** | **87.11** |
| Ru | Tl | 0.228 | 86.9 |
| Ru | Rh | 0.121 | 86.2 |
| Ru | Pd | 0.099 | 85.56 |
| Ru | Ni | 0.216 | 84.76 |
| Ru | Pt | 0.159 | 84.7 |
| Ru | Mn | 0.24 | 83.87 |
| Ru | Hg | 0.27 | 83.17 |
| Ru | Cu | 0.209 | 81.1 |
| Ru | Ag | 0.196 | 80.7 |
| Ru | Co | 0.214 | 78.53 |
| **Ru** | **Ru** | **0.302** | **85.2** |
| Ru | Sc | 0.304 | 83.91 |
| Ru | Bi | 0.312 | 17.57 |
| Ru | In | 0.322 | 90.85 |
| Ru | Cd | 0.332 | 86.48 |
| Ru | Nb | 0.357 | 86.35 |

| | | | |
|---|---|---|---|
| Ru | Pb | 0.371 | 19.79 |
| Ru | Zr | 0.379 | 86.72 |
| Ru | Y | 0.493 | 12.28 |
| Ru | Tc | 0.504 | 99.08 |
| Ru | Ta | 0.538 | 83.76 |
| Ru | Mo | 0.604 | 83.56 |
| Ru | Os | 0.613 | 96.06 |
| Ru | Fe | 0.618 | 84.62 |
| Ru | V | 0.622 | 84.75 |
| Ru | W | 0.732 | 83.38 |
| Ru | Re | 0.769 | 95.26 |

# S3 Experimental Methods

### Chemicals

Ruthenium chloride hydrate, (RuCl3·xH2O); chromium (iii) chloride anhydrous 99.99% trace metals basis (CrCl2); Titanium diisopropoxide bis(acetylacetonate) 75wt. % in isopropanol; and Propylene oxide (≥99.5% GC) were all purchased from Sigma-Aldrich. Nafion® (5 wt% in a mixture of lower aliphatic alcohols and water) and AvCarb MGL190 were used for electrode preparation and were purchased from the Fuel Cell Store. All chemicals were used without any further purification.

### Synthesis

The samples were synthesized using a sol-gel procedure [14] by dissolving a total amount of 2.7 mmol metal precursors in 4 mL ethanol. The solution is sonicated in a water bath for 30 mins until it is clear. Then, it was chilled in a refrigerator for 2 hours to prevent any undesired hydrolysis and condensation which may affect the gelation process. Afterward, 2 mL of propylene oxide was added dropwise to the mixture while the solution was stirred using a magnetic bar. The solution was aged for 1 day to promote gel formation and then washed with acetone. The powder was finally extracted by drying the gel in a vacuum oven for 1 day and annealing at 400°C for 2 hours to produce a rutile crystal structure.

### XRD

X-ray Diffraction (XRD) was conducted on a Miniflex 600 (Rigaku, Japan) equipped with D/tex Ultra silicon trip detector and Cu Kα (λ = 1.5418 Å) radiation source. Powders were prepared by mixing with methanol and then dropping a small drop of the mixture to fill a 4 mm diameter x 100 μm deep groove in a single crystal silicon holder (zero-background). The angle was varied between 20° to 80° with a step size of 0.05° every 2 seconds.

To evaluate the nanocrystalline size of the electrocatalysts, we used Scherrer's equation:

$$Crystallite\ Size: D = \frac{K\lambda}{FWHM cos cos\ \theta}$$

D is the mean crystallite size, l is 0.154 nm for Cu X-ray source, K is shape factor has a typical value between 0.9-1. The full-width half-maximum (FWHM) of the peaks were measured by fitting to Gaussian distribution and then calculated from the standard deviation (σ) using the following relation:

$$FWHM = 2\sqrt{2.ln2} \approx 2.355\,\sigma$$

**Table S3.** XRD peaks positions and crystallite size (D) of the samples

| | Position (degree) | | D (nm) | |
|---|---|---|---|---|
| Sample | (110) | (101) | (110) | (101) |
| $RuO_x$ | 27.910 | 35.020 | 6.120 | 7.845 |
| $Ru_{0.75}Cr_{0.25}O_x$ | 28.035 | 35.675 | 3.602 | 4.994 |
| $Ru_{0.6}Cr_{0.2}Ti_{0.2}O_x$ | 28.075 | 35.810 | 3.525 | 4.827 |

**Electron Microscopy**

Transmission electron microscopy (TEM) was performed in a Hitachi HF3300 and Tecnai Titan equipped with a cold field-emission electron gun using an accelerating voltage of 300 kV. TEM bright-field images were used to determine the size and shape of nanoparticles. Electron energy loss spectrometer (EELS) was used in scanning transmission electron microscopy (STEM) mode to analyze and quantify the elemental composition of the nanoparticles. Also, a secondary electron (SE) detector was used to collect high-resolution images of the morphology of the nanoparticles. Powder samples were prepared by dispersing 1 mg of the sample in 10 ml ethanol to form an ink, the ink was sonicated for 10 minutes before drop-casting a 1 -2 µL drop on a 400-mesh holey carbon copper grid and drying overnight.

**ICP-AES**

The dissolution rate of the catalysts was investigated using iCAP™ PRO XP ICP-OES.

Samples for ICP analysis were prepared by drawing a 5 mL volume of the electrolyte from the electrochemical cell from both the cathode and anode chambers. Multielement standards (High Purity Standards, ICP-MS-68B-A) were used to calibrate and analyze Cr and Ti, and Ru standard (Specpure®, Ru 1000µg/ml, Alfa Aesar) to calibrate and analyze Ru. Elemental standards were prepared in concentrations of 0.1, 1, 10, and 100 ppm for calibration.

**Electrochemical testing**

Three-electrode test

Three-electrode tests were carried out in an H-cell configuration using a Nafion 117 membrane separating the cathode and the anode electrolyte compartments. A graphite rod was used as a counter electrode and $Hg/Hg_2SO_4$ (MSE) as a reference electrode. The anolyte was continuously purged with Ar to displace $O_2$ and improve bubble release from the surface of the electrocatalyst.

The cell was connected to a BioLogic VSPe-300 potentiosat for measurement. All potentials were iR-corrected by measuring the solution resistance from electrochemical impedance spectroscopy (EIS) with a bias of 1.53V vs. RHE in the frequency range from 100 kHz to 10 MHz and an amplitude of 5 mV. All the potentials in this study were reported with respect to a reversible hydrogen electrode (RHE) using the following relationship:

$$E_{RHE} = E_{Hg/Hg_2SO_4} + 0.640 + 0.0591 \times pH$$

Sample preparation

Electrocatalyst inks were prepared by mixing the powder with a solution of 1:1 water to ethanol and a 5 wt.% Nafion binder. The ink was then air sprayed using $N_2$ courier on one side of a 1 cm x 1 cm AvCarb MGL190 carbon and left to dry in the air.

Intrinsic Activity

The electrochemical surface area (ECSA) was calculated by measuring the double-layer capacitance ($C_{dl}$) of the electrocatalyst using cyclic voltammetry (CV). Three CV scans were acquired at each potential sweeping rate from 20-100 $mV.s^{-1}$ with 20 $mV.s^{-1}$ increment steps.

The difference between anodic and cathodic current density for the third CV cycle of each sweeping rate is calculated and plotted as a function of the sweeping rate. The data points are then fitted to a line where the slope is equal to $C_{dl}$. Finally, ECSA is calculated by dividing $C_{dl}$ over a specific capacitance value ($C_s$) that can range between 0.02-0.13 $mF.cm^{-2}$. In this work, we used 0.04 $mF.cm^{-2}$**.**

**X-ray absorption spectroscopy**

X-ray absorption spectroscopy (XAS) measurements for the K-edge of Ru, Ti, and Cr were carried out at 20BM in the advanced photon source (APS, IL, USA). A custom-made electrochemical cell with a three-electrode configuration was used to collect XAS spectra *in situ* during OER. A graphite rod and Ag/AgCl electrode were used as counter electrode and reference electrode, respectively. The catalyst was prepared on one side of a carbon paper while the other side was adhered to a thin Kapton tape (polyimide film with silicone adhesive) and connected electrically by Cu tape. Then, the prepared sample was mounted on the electrochemical cell so that the backside of the sample is facing the beam and the catalyst (front side) is in direct contact with the electrolyte.

All measurements were done in air and under ambient conditions. *In situ* experiments were conducted at 4 conditions: Dry, OCP, 1.1V (Before OER) and 1.4V (during OER) in 0.5M $H_2SO_4$. Data was collected in fluorescence mode using a Passivated Implanted Planar Silicon (PIPS)/Lytle detector placed at 45° degrees. Five spectra were collected and averaged at each condition to improve the quality of the data and increase the signal to noise ratio. Data post-processing and fitting was done entirely using Demeter software package. [15]

**Scanning transmission X-ray microscopy**

STXM and ptychography measurement were conducted at the SM beamline of the Canadian light source (CLS).[16] A 35 nm outermost-zone plate was used for both data acquisition modes. The diffraction-limited spatial resolution of the conventional STXM is about 30 nm, while the

ptychography has a spatial resolution about 10 nm. The samples were raster-scanned with synchronized detection of transmitted X-rays by a scintillator-coupled photomultiplier tube (PMT) for the conventional STXM measurement and by a CCD area detector (Andor™ DX434-BN, 1024x1024 pixels, 13 μm pixel size) to acquire diffraction images for the ptychography measurement. For ptychography, the real-space images (absorption and phase contrast) were reconstructed by the in-house developed software PyPIE.[17] Chemical imaging and XANES spectra were obtained using STXM or ptychography image sequence (stack) scans over a range of photon energies for interested elemental edges.[18] Both STXM and ptychography X-ray absorption images were analyzed using the aXis2000 software package, which allows for detailed interactive processing of the images and extracting of the X-ray absorption spectra at sample regions of interest. Finally, chemical imaging was conducted by fitting the STXM or ptychography image stacks using the internal reference spectra from the image stacks.

**In situ differential electrochemical mass spectroscopy (DEMS)**

The experimental setup consists of two interconnected vacuum chambers, one with a high vacuum and the other with a mild vacuum. The latter is connected to an electrochemical cell that operates at ambient pressure, allowing in-situ generated oxygen to be drawn into the vacuum chamber for mass spectrometer analysis. The working electrode is a gold film sputtered on a porous polytetrafluoroethylene membrane that allows gas flow while rejecting liquid. A cold trap cooled with dry ice is installed between the electrochemical cell and the vacuum chamber to prevent water vapor from damaging the mass spectrometer. The catalyst is applied to the gold film as an ink, which is then dried. The electrochemical cell is a typical three-electrode system with a volume of approximately 1 mL, suitable for isotope experiments. Chronoamperometry at 1.8 (vs. RHE) is performed for 5 mins on the catalysts in a 0.5 M sulfuric acid electrolyte labeled with $H_2{}^{18}O$, while the mass signals of the gaseous products

$^{32}O^2$, $^{34}O^2$, and $^{36}O^2$ are recorded. Prior to the electrochemical measurements, all electrolytes are purged with high-purity argon to remove dissolved oxygen.

# S4 Experimental Figures

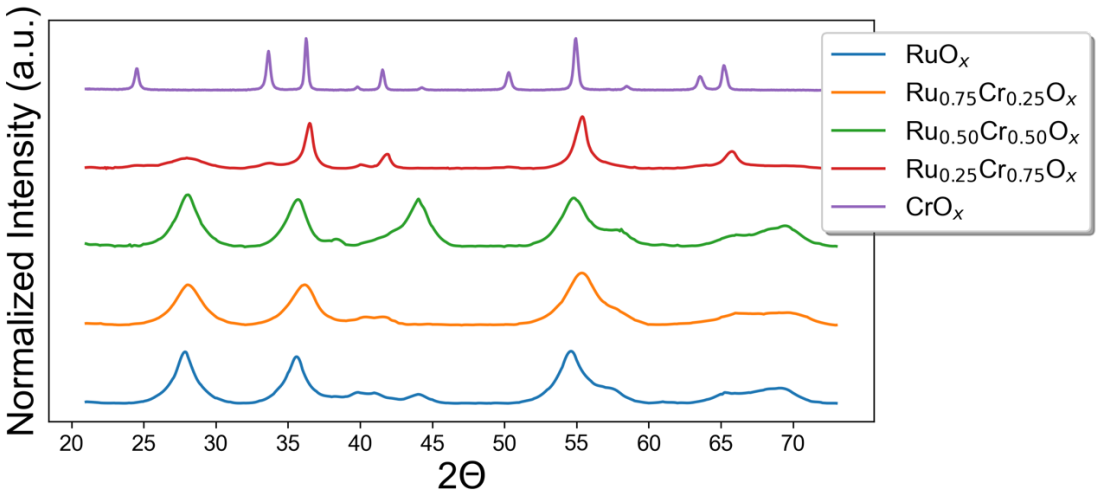


**Figure S3.** XRD of synthesized $Ru_yCr_{1-y}O_x$ samples compared to a commercial $RuO_2$ standard. CrOx characteristic peaks match with $Cr_2O_3$.

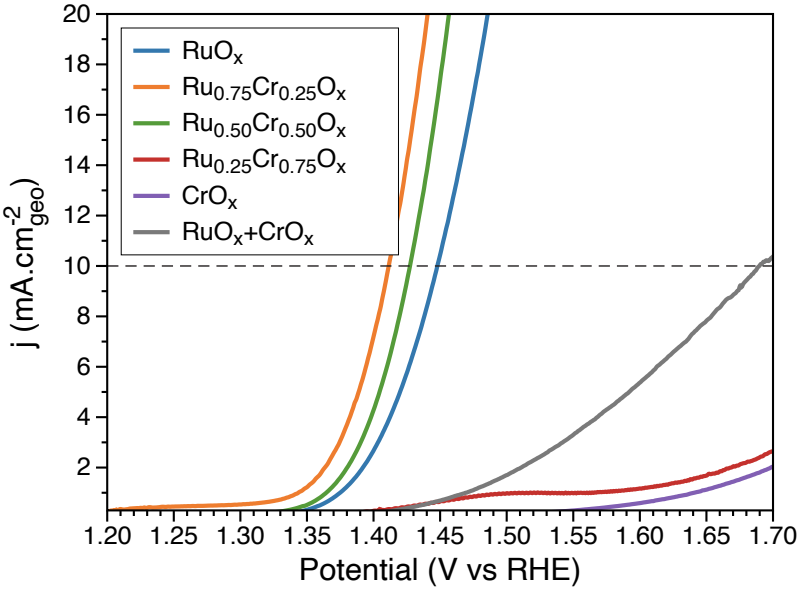


**Figure S4.** Polarization curve of synthesized $Ru_yCr_{1-y}O_x$ samples.

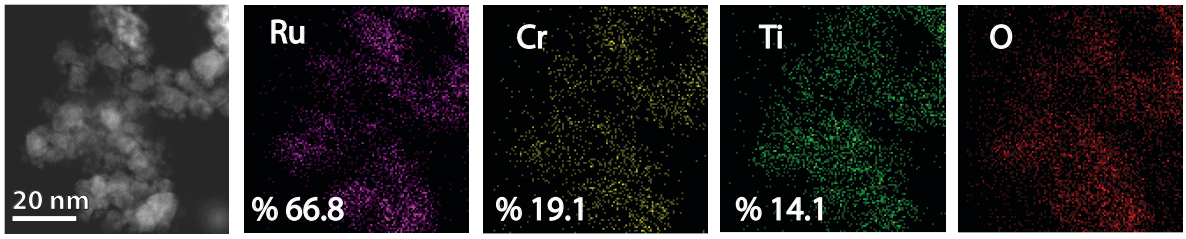


**Figure S5.** Cyclic voltammetry scan for synthesized samples.

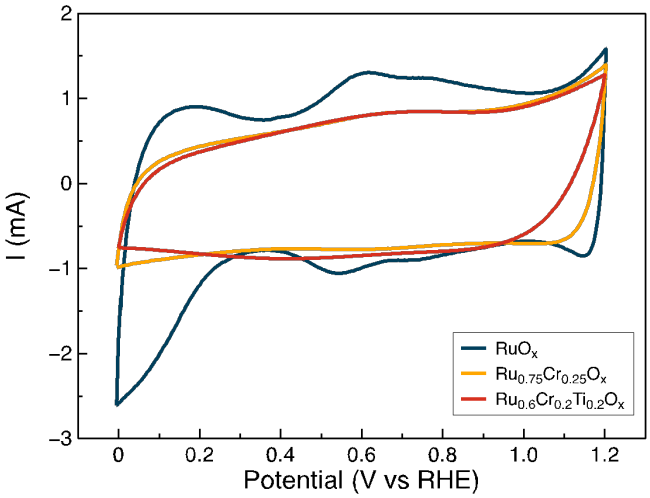


**Figure S6.** Cyclic voltammetry scan for synthesized samples.

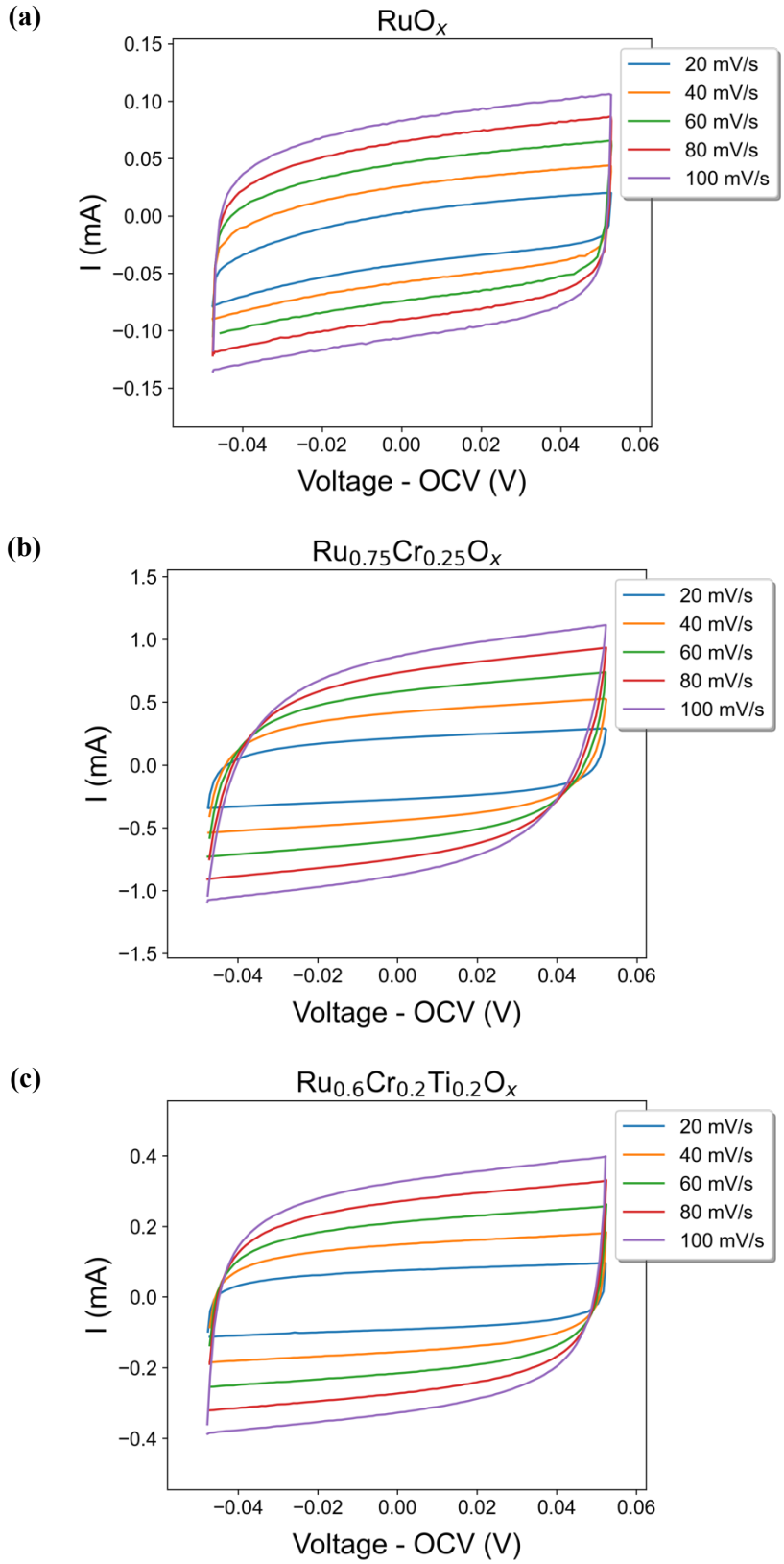


**Figure S7.** Cyclic voltammetry (CV) curves collected at non-Faradaic region for synthesized samples at various potential scan rates.

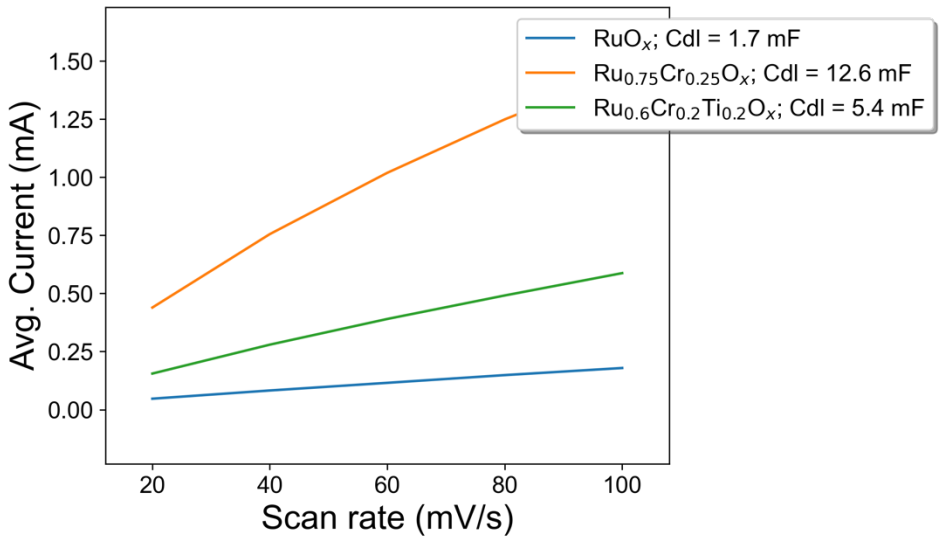


**Figure S8.** Anodic current density plotted as a function of potential scan rate to calculate. The slope of the linear fit gives the double layer capacitance (Cdl) of synthesized samples.

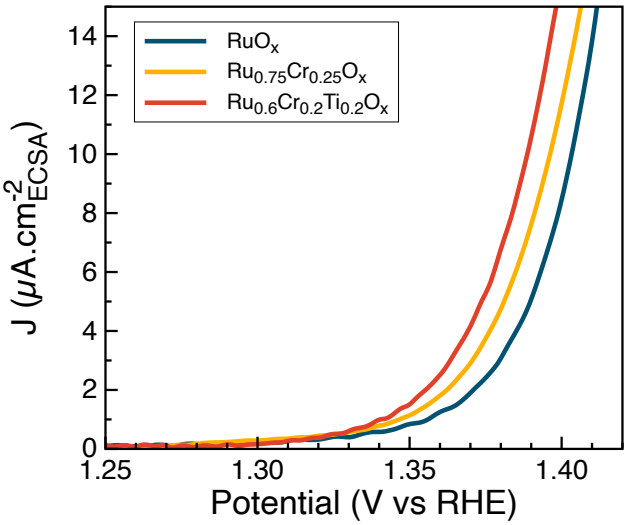


**Figure S9.** Polarization curves of synthesized samples normalized by the electrochemical surface area (ECSA) of Ru sites compared to a commercial $RuO_2$ standard.

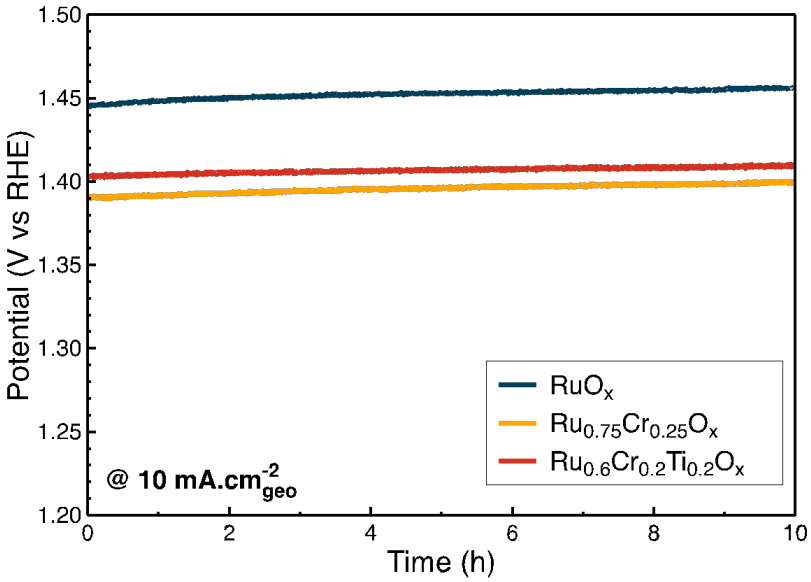


**Figure S10.** Three-electrode chronopotentiometry test of synthesized samples at 10 $mA.cm_{geo}^{-2}$ in 0.5M $H_2SO_4$.

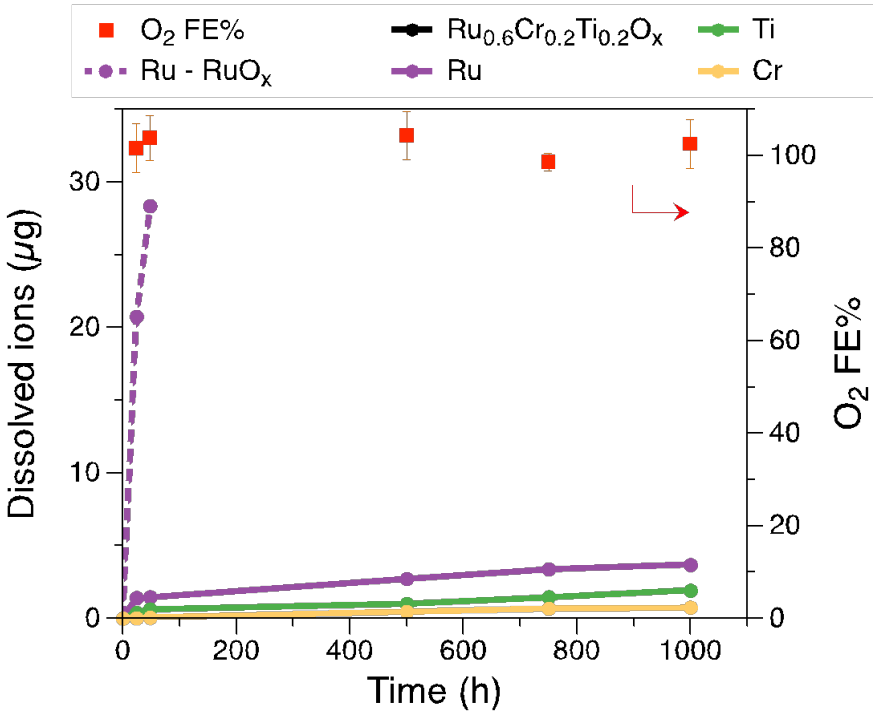


**Figure S11.** Accumulative total dissolved ions (μg) for $RuO_x$ and $Ru_{0.6}Cr_{0.2}Ti_{0.2}O_x$ after OER @10 mA/cm$^2$ in 0.5 M $H_2SO_4$.

(a) (b)

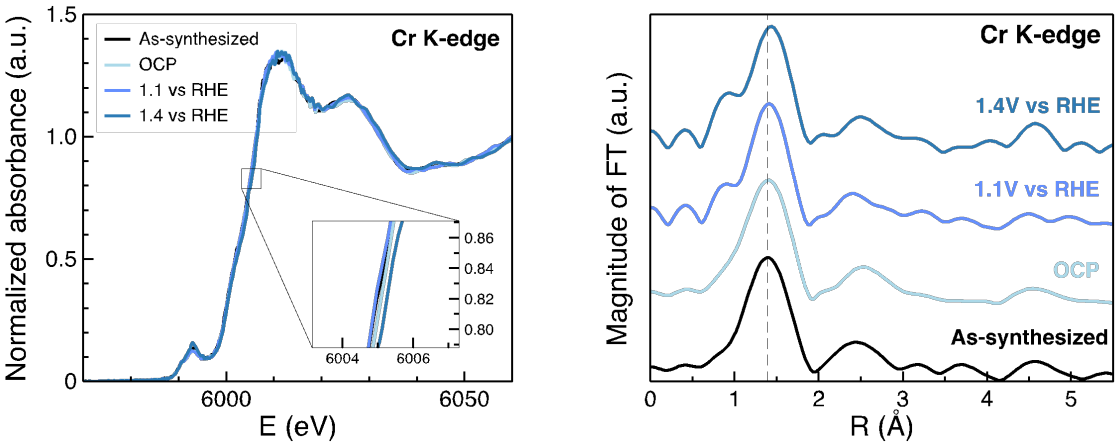


**Figure S12.** Cr K-edge a) XANES spectrum and b) Fourier transform of the $k^2$-weighted EXAFS of $Ru_{0.6}Cr_{0.2}Ti_{0.2}O_x$ as-synthesized, at open circuit potential (OCP), pre-OER (1.1V vs RHE), and during-OER (1.4V vs RHE).

(a) (b)

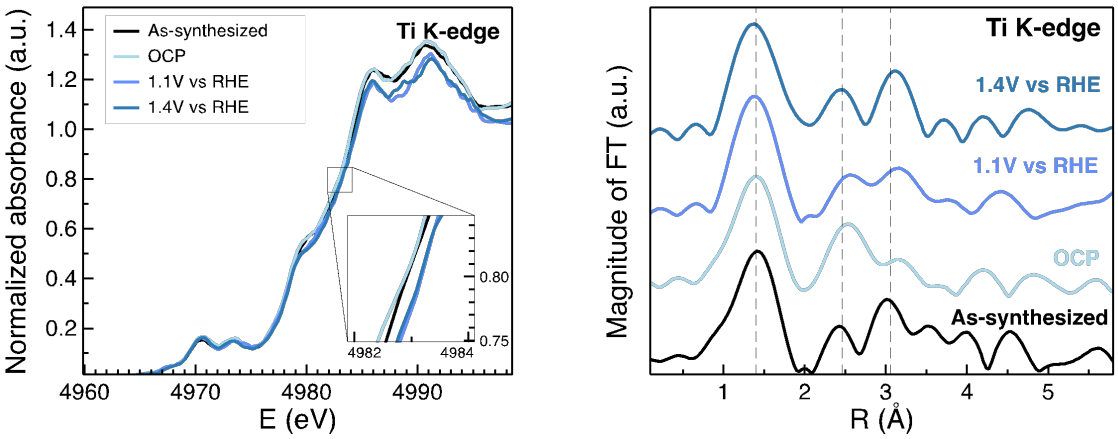


**Figure S13.** Ti K-edge a) XANES spectrum and b) Fourier transform of the $k^2$-weighted EXAFS of $Ru_{0.6}Cr_{0.2}Ti_{0.2}O_x$ as-synthesized, at open circuit potential (OCP), pre-OER (1.1V vs RHE), and during-OER (1.4V vs RHE).

(a) (b)

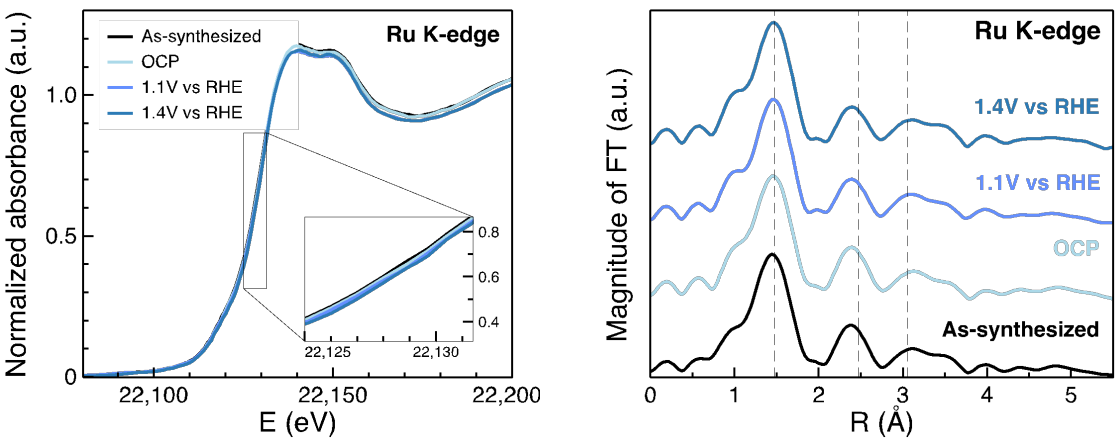


**Figure S14.** Ru K-edge a) XANES spectrum and b) Fourier transform of the $k^2$-weighted EXAFS of $Ru_{0.6}Cr_{0.2}Ti_{0.2}O_x$ as-synthesized, at open circuit potential (OCP), pre-OER (1.1V vs RHE), and during-OER (1.4V vs RHE).

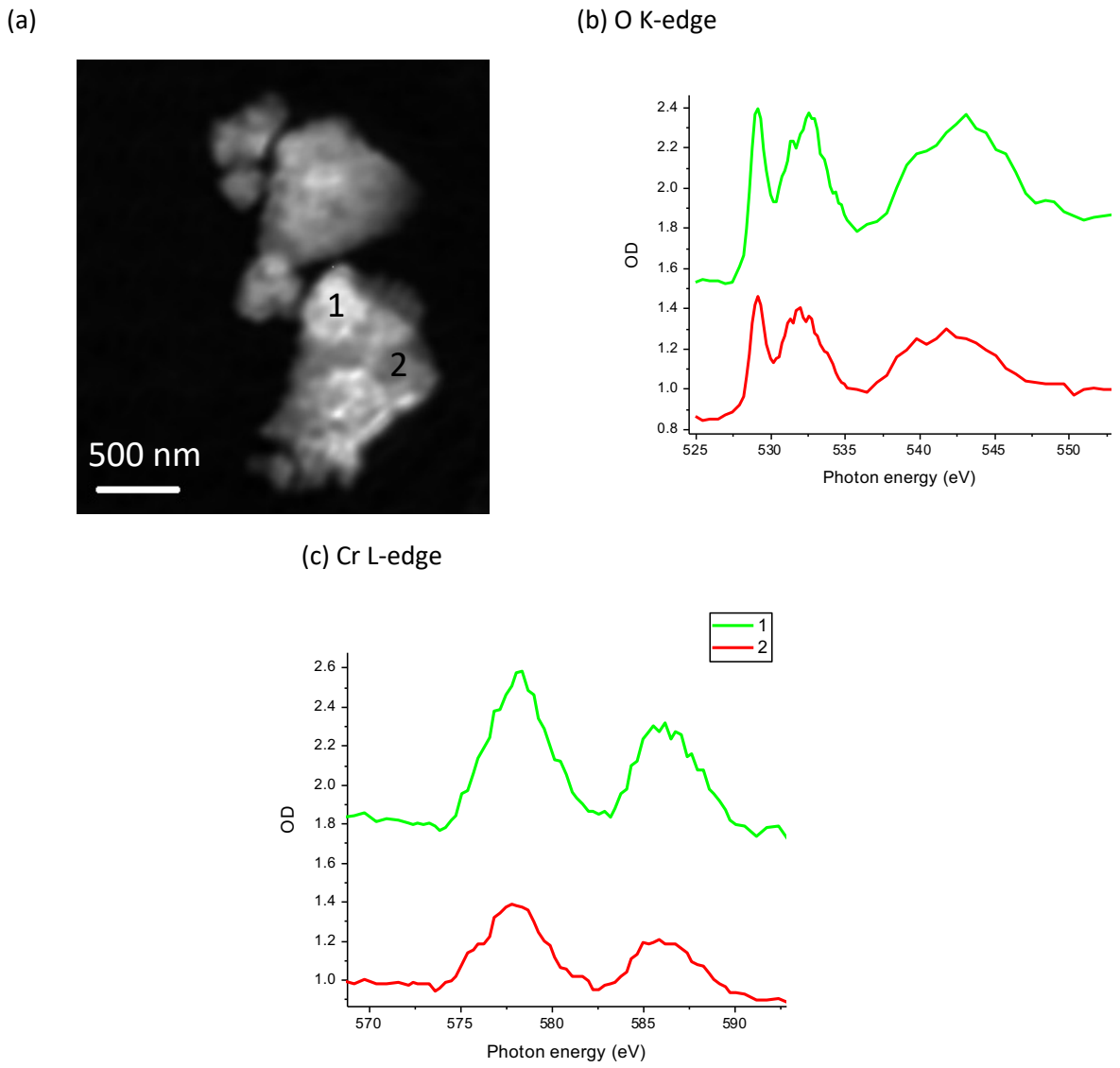


**Figure S15.** Scanning transmission X-ray microscope analysis of $Ru_{0.75}Cr_{0.25}O_x$ a) X-ray fluorescence map averaged 568-594 eV. Two regions are identified 1: bright region representing thick agglomerated sampling point, 2: thin sampling point. Soft X-ray absorption spectrum are collected from each sampling point for b) O K-edge and c) Cr L-edge

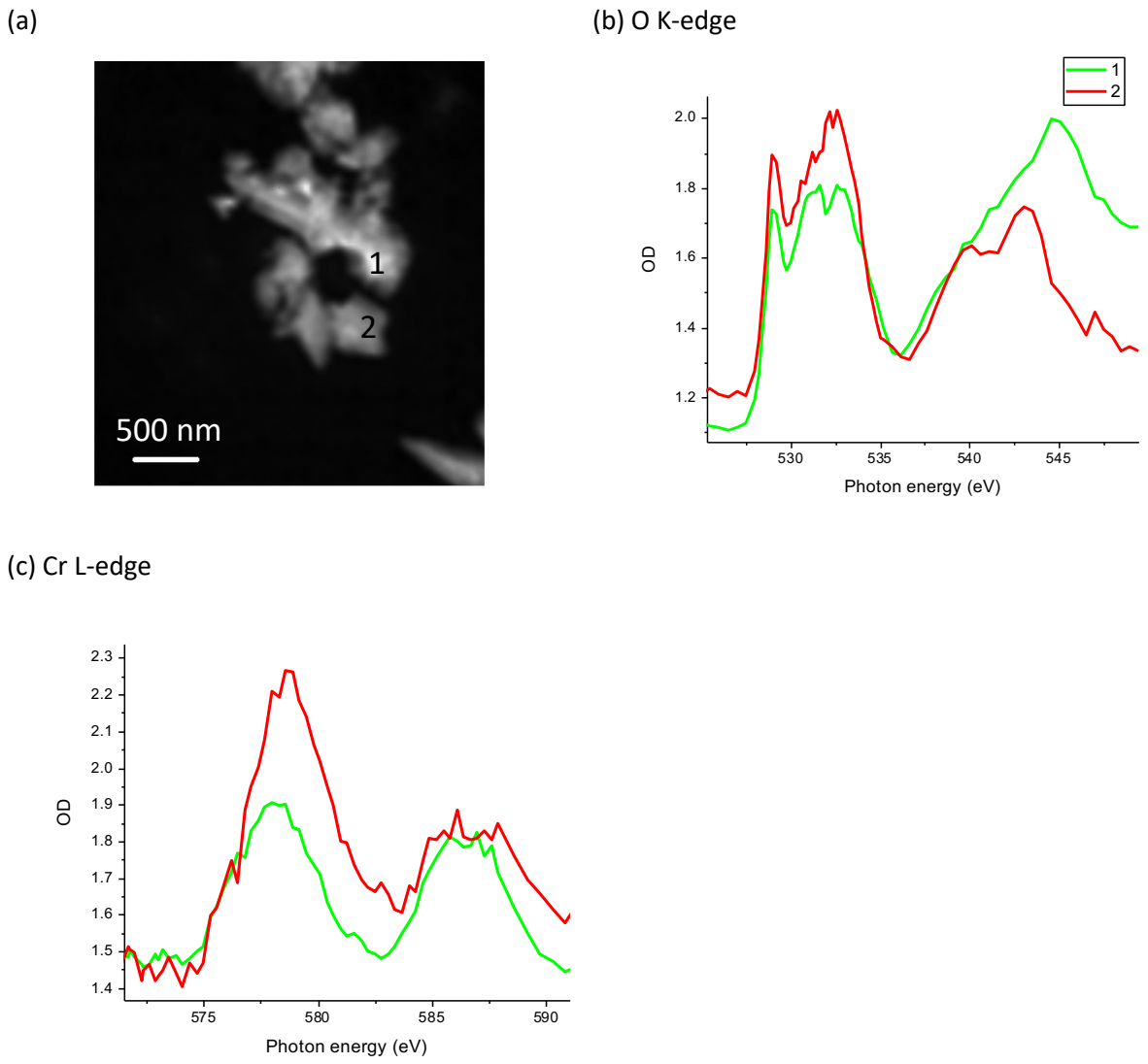


**Figure S16.** Scanning transmission X-ray microscope analysis of $Ru_{0.6}Cr_{0.2}Ti_{0.2}O_x$ a) X-ray fluorescence map averaged 452-476 eV. Two regions are identified 1: bright region representing thick agglomerated sampling point, 2: thin sampling point. Soft X-ray absorption spectrum are collected from each sampling point for b) O K-edge, c) Cr L-edge.

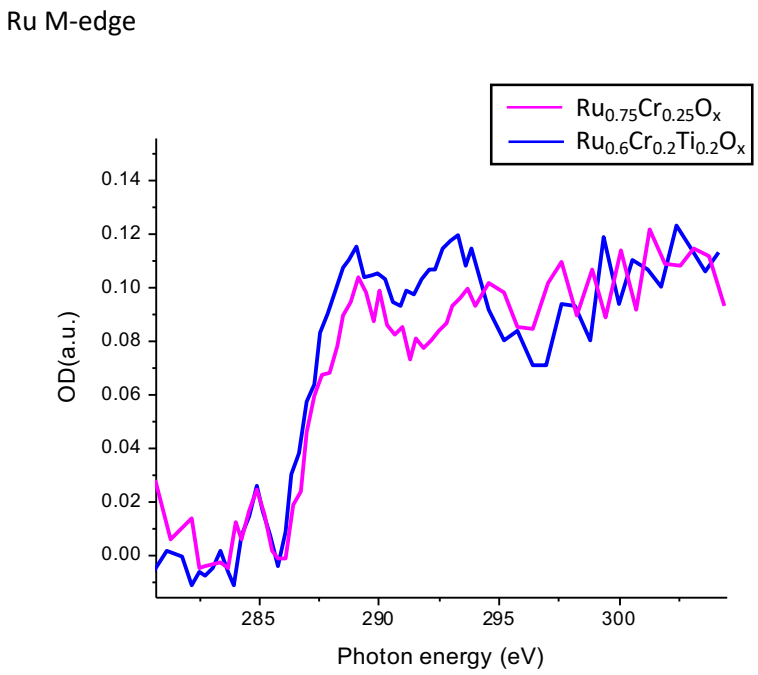


**Figure S17.** Ru M-edge XANES comparison between $Ru_{0.75}Cr_{0.25}O_x$ and $Ru_{0.6}Cr_{0.2}Ti_{0.2}O_x$

# S5 Experimental Tables

**Table S4.** Total ions dissolved for $RuO_x$ and $Ru_{0.6}Cr_{0.2}Ti_{0.2}O_x$ after OER @10 mA/cm$^2$ in 0.5 M $H_2SO_4$.

| Catalyst | | 24h | | 48h | | 500h | | 750h | | 1000h | |
|---|---|---|---|---|---|---|---|---|---|---|---|
| | | ⊗⌈g | ⊗wt. % | ⊗⌈g | ⊗wt. % | ⊗⌈g | ⊗wt. % | ⊗⌈g | ⊗wt. % | ⊗⌈g | ⊗wt. % |
| **$RuO_x$** | Ru | **-20.75 (**±2.0%) | -5.46 | **-28.36 (**±2.1%) | -7.47 | - | - | - | - | - | - |
| **$Ru_{0.6}Cr_{0.2}Ti_{0.2}O_x$** | Ru | **-1.41 (**±8.8%) | -0.62 | **-1.45 (**±6.0%) | -0.64 | **-2.27 (**±3.8%) | -1.19 | **-3.38 (**±2.9%) | -1.48 | **-3.68 (**±2.7%) | -1.61 |
| | Ti | **-0.38 (**±3.2%) | -1.07 | **-0.64 (**±3.2%) | -1.76 | **-1.00 (**±2.9%) | -2.77 | **-1.46 (**±4.2%) | -4.05 | **-1.91 (**±1.4%) | -5.30 |
| | Cr | **-0.034 (**±5.8%) | -0.01 | **-0.065 (**±5.8%) | -0.02 | **-0.48 (**±6.6%) | -0.12 | **-0.68 (**±7.7%) | -0.18 | **-0.75 (**±6.3%) | -0.20 |

## Overall performance

**Table S5.** A summary table of Ir-free OER catalyst performance in acidic electrolyte <300 mV overpotential from literature.

| Catalyst | $\eta_{iR}$ @10 mA/cm$^2$ (mV) | $\eta_{iR}$ @100 mA/cm$^2$ (mV) | Stability @ 10 mA/cm$^2$ (h) | Stability @ 100 mA/cm$^2$ (h) | Ref. |
|---|---|---|---|---|---|
| **$Ru_{0.6}Cr_{0.2}Ti_{0.2}O_x$** | **172** | **267** | **1100 (+8 mV)** | **200 (+5 mV)** | **This work** |
| **$Ru_{0.6}Cr_{0.4}O_x$** | **159** | **246** | | | **This work** |
| $Ru_{0.7}W_{0.2}Er_{0.1}O_x$ | 168 | 240 | 500 (+83 mV) | 120 | *Nat. Comm., 2020, 11:5368* |
| $Ru_1$-$Pt_3Cu$ | 220 | - | 28 | - | *Nat. Catal.*, 2019, 2:304. |
| $Ru_{0.4}Cr_{0.6}O_2$ | 178 | - | 10 | - | *Nat. Commun.*, 2019, 10:162. |
| $Sr_{0.9}Na_{0.1}RuO_3$ | 170 | - | - | - | *Nat. Commun.*, 2019, 10:2041. |
| Au-Ru branches | 220 | - | - | - | *Angew. Chem. Int. Ed.*, 2018, 57:10241. |
| UfD-$RuO_2$/CC | 179 | - | 20 | - | *Adv. Energy Mater.*, 2019, 9:1901313. |
| Cu-doped $RuO_2$ | 188 | - | 8 | - | *Adv. Mater.*, 2018, 30:1801351. |

# S6 Surface Pourbaix DFT Figures

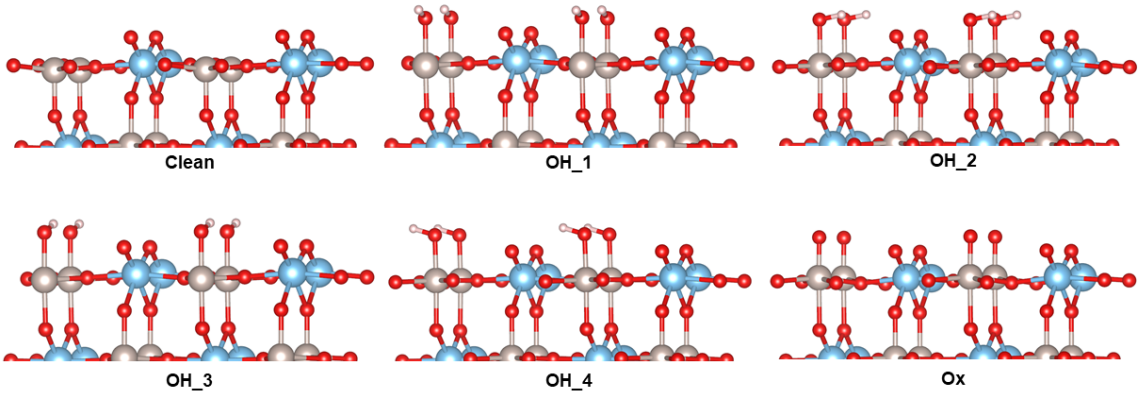


**Figure S17.** $RuTiO_4$ (101) surface Pourbaix Diagram Intermediates: From Clean (Top-Left), OH* rotation screening (1-4) and O*

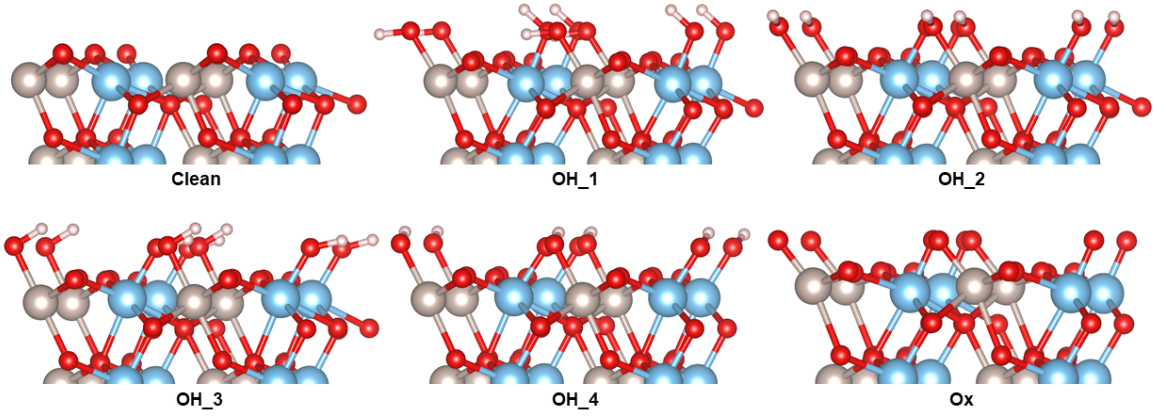


**Figure S18.** $RuTiO_4$ (101) surface Pourbaix Diagram Intermediates: From Clean (Top-Left), OH* rotation screening (1-4) and O*

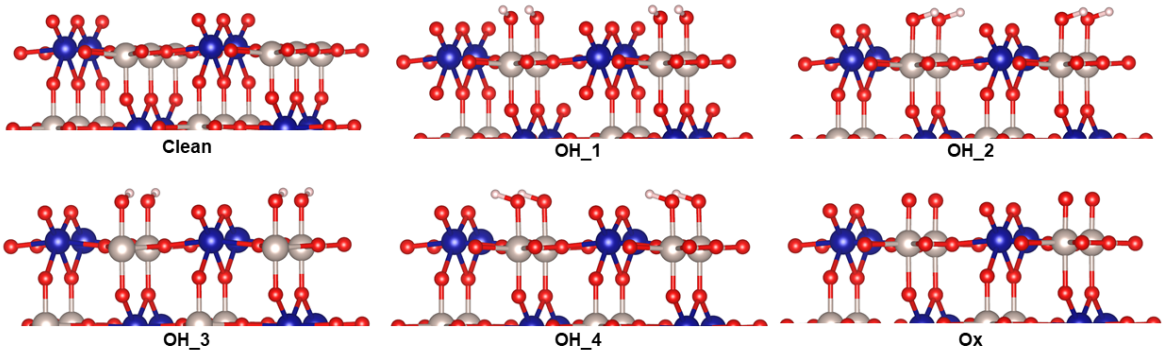


**Figure S19.** $RuCrO_4$ (110) surface Pourbaix Diagram Intermediates: From Clean (Top-Left), OH* rotation screening (1-4) and O*

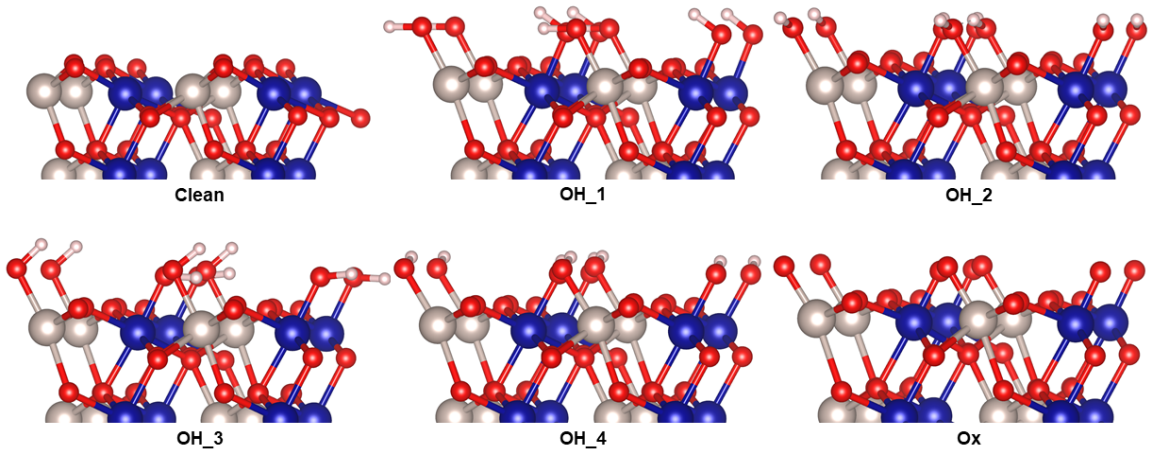


**Figure S20.** $RuCrO_4$ (101) surface Pourbaix Diagram Intermediates: From Clean (Top-Left), OH* rotation screening (1-4) and O*

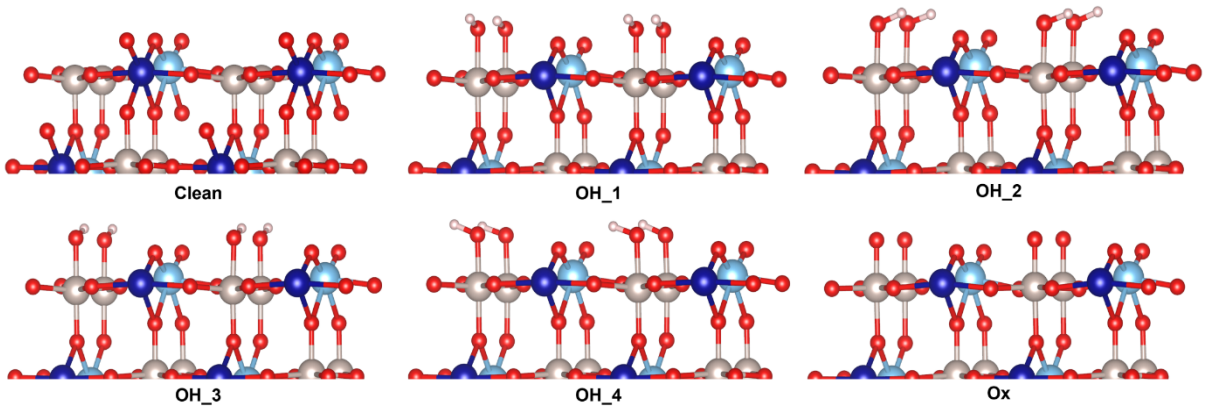


**Figure S21.** $RuCrTiO_x$ (110) surface Pourbaix Diagram Intermediates: From Clean (Top-Left), OH* rotation screening (1-4) and O*

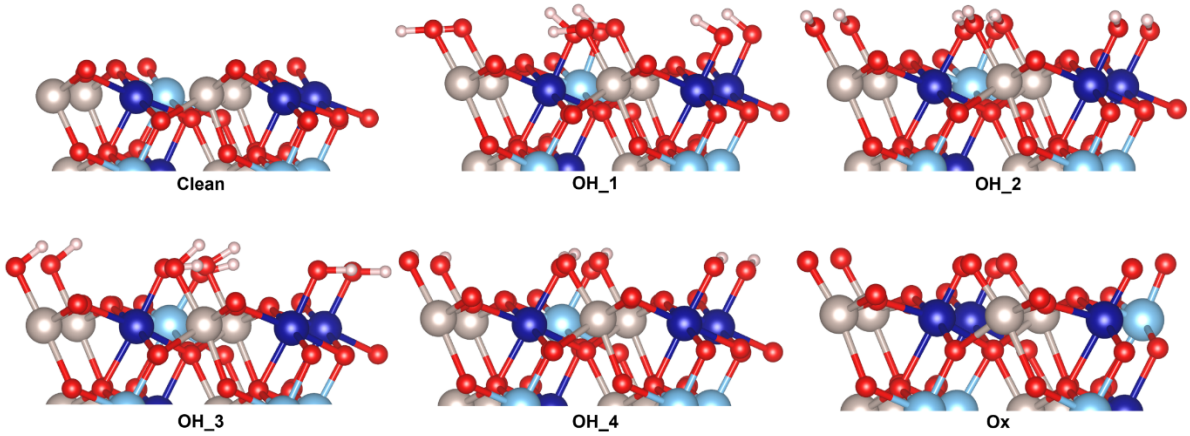


**Figure S22.** $RuCrTiO_x$ (101) surface Pourbaix Diagram Intermediates: From Clean (Top-Left), OH* rotation screening (1-4) and O*

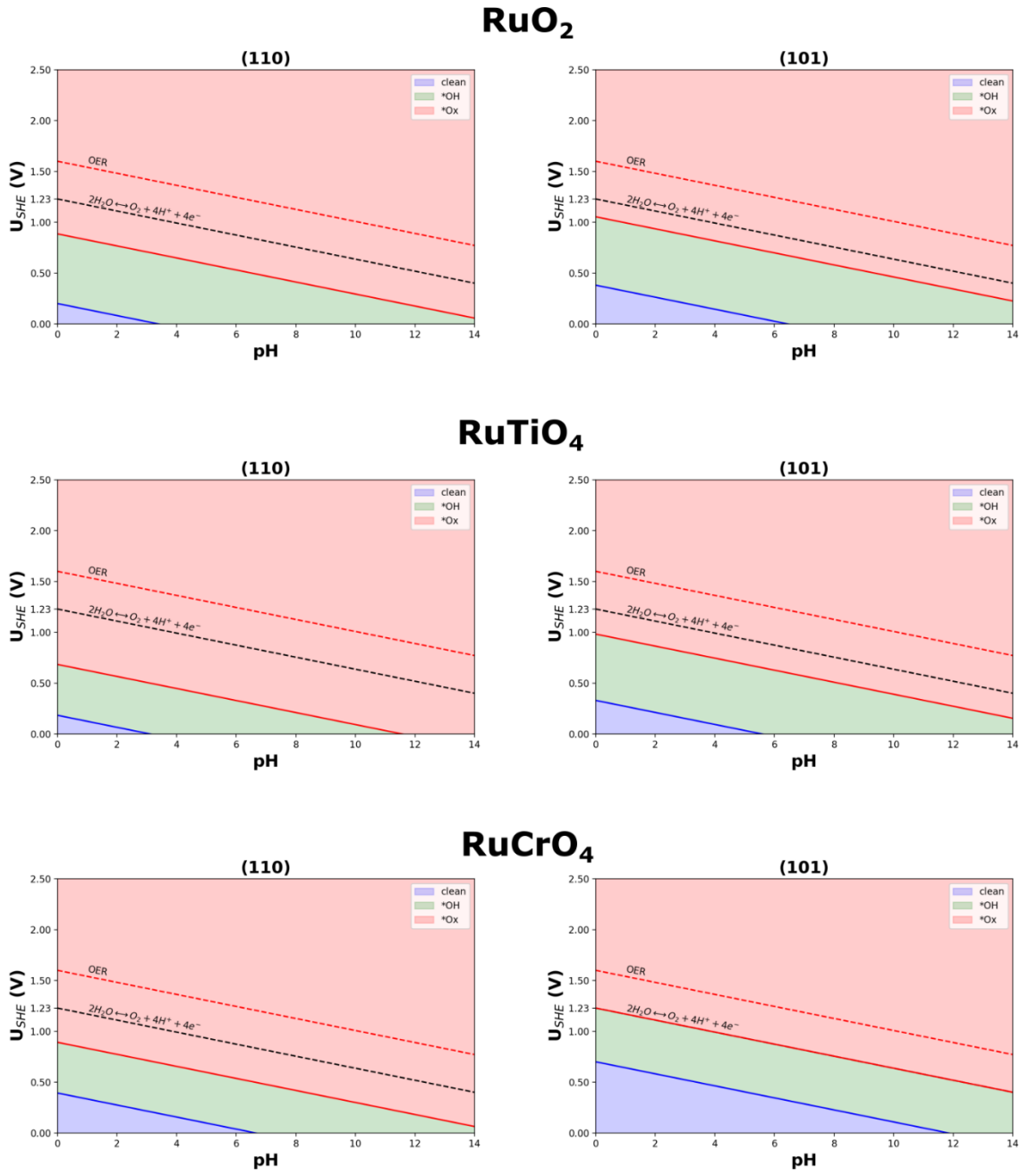


**Figure S23.** $RuO_2$, $RuTiO_4$, and $RuCrO_4$ for both (110) and (101) surface Pourbaix Diagrams with clean (blue), OH*(green) and O*(red) terminated regions. The black dashed line is the standard OER potential line starting at 1.229 V and the red dashed line starting at 1.60 V as selected in this work.

# S7 OER Intermediates DFT Figures

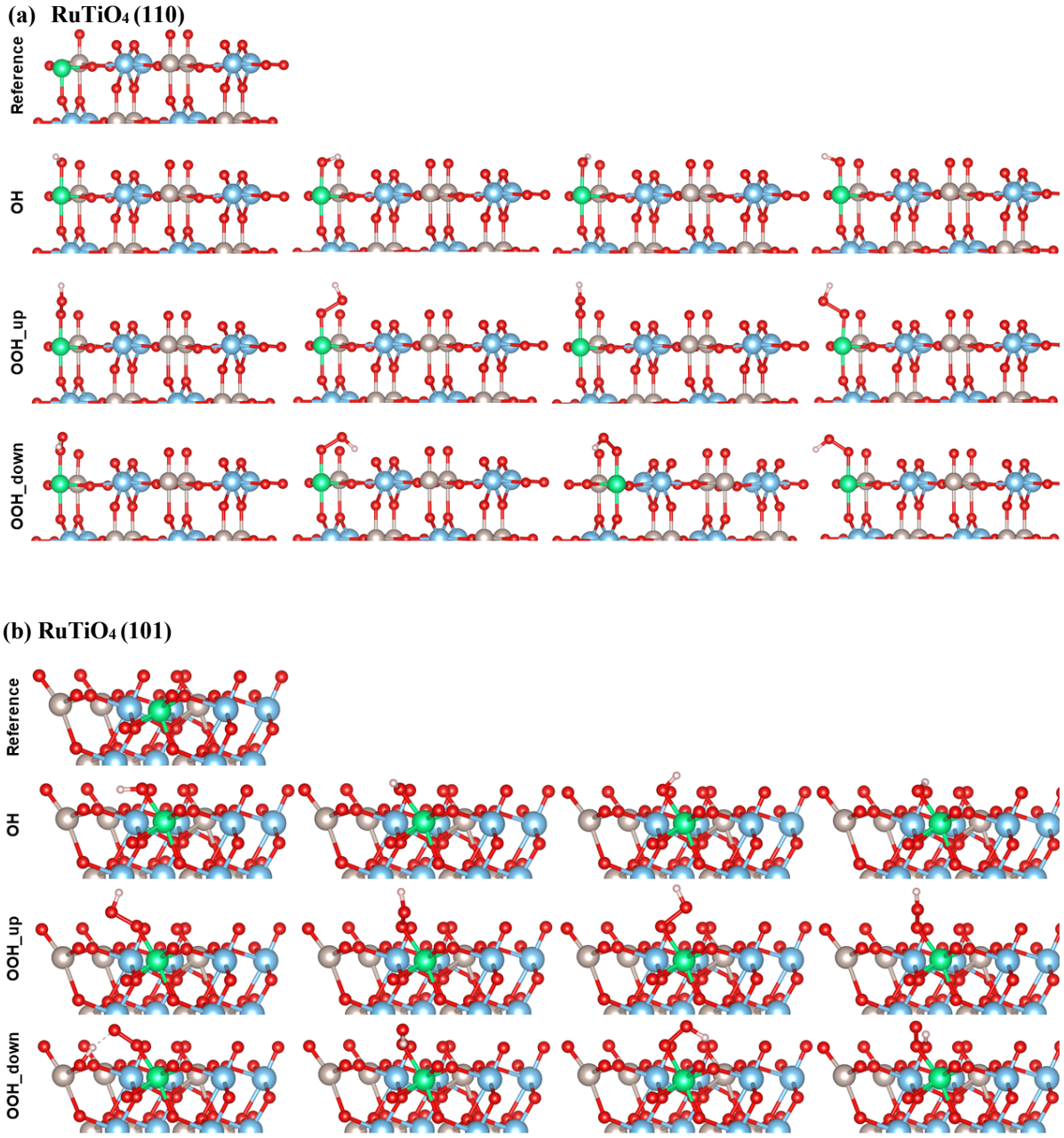


**Figure S24.** $RuTiO_4$ OER Intermediates: From Reference to OH, $OOH_{up}$, and $OOH_{down}$ (1-4) rotations. (*) Green color represents the active site on top of the surface.

**(a) $RuCrO_4$ (110)**

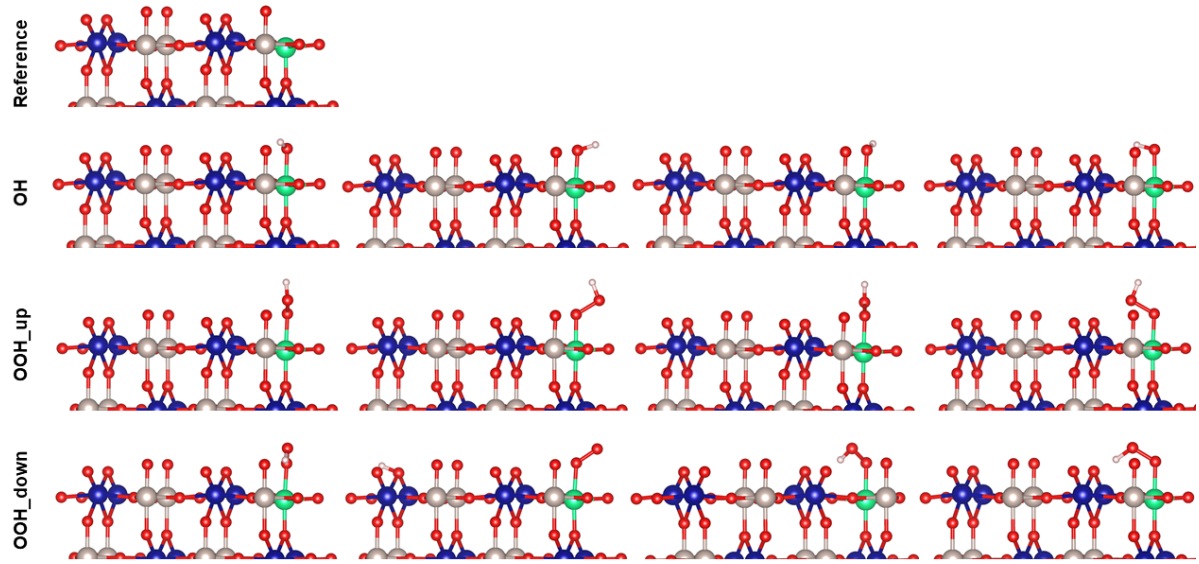


**(b) $RuCrO_4$ (101)**

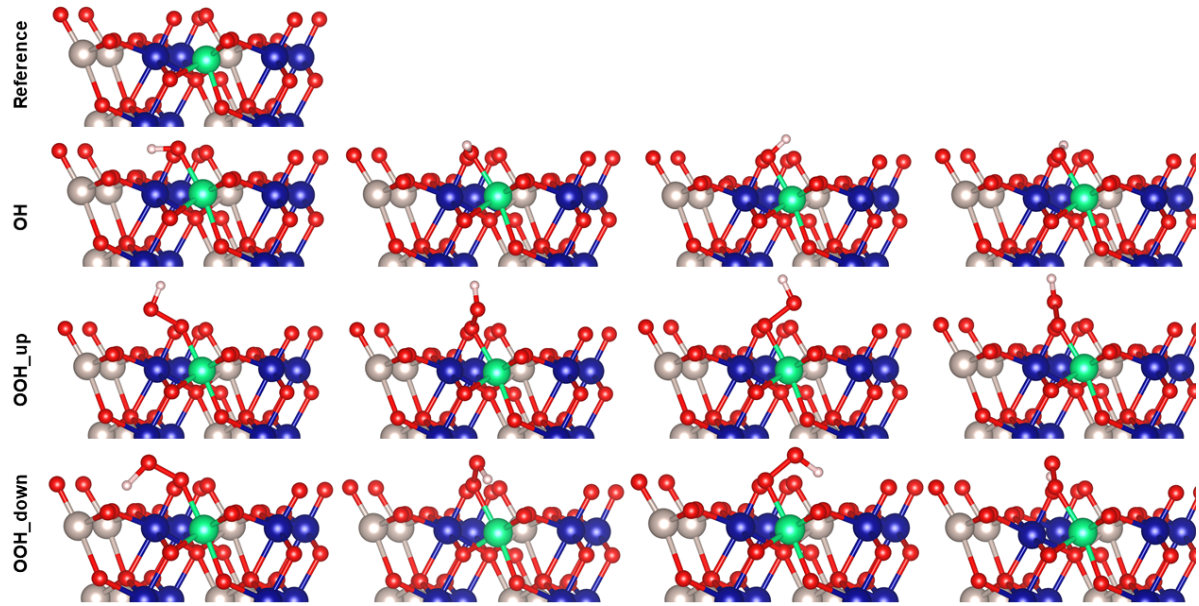


**Figure S25.** $RuCrO_4$ OER Intermediates: From Reference to OH, $OOH_{up}$, and $OOH_{down}$ (1-4) rotations. (*) Green color represents the active site on top of the surface.

**(a) $RuCrTiO_x$ (110)**

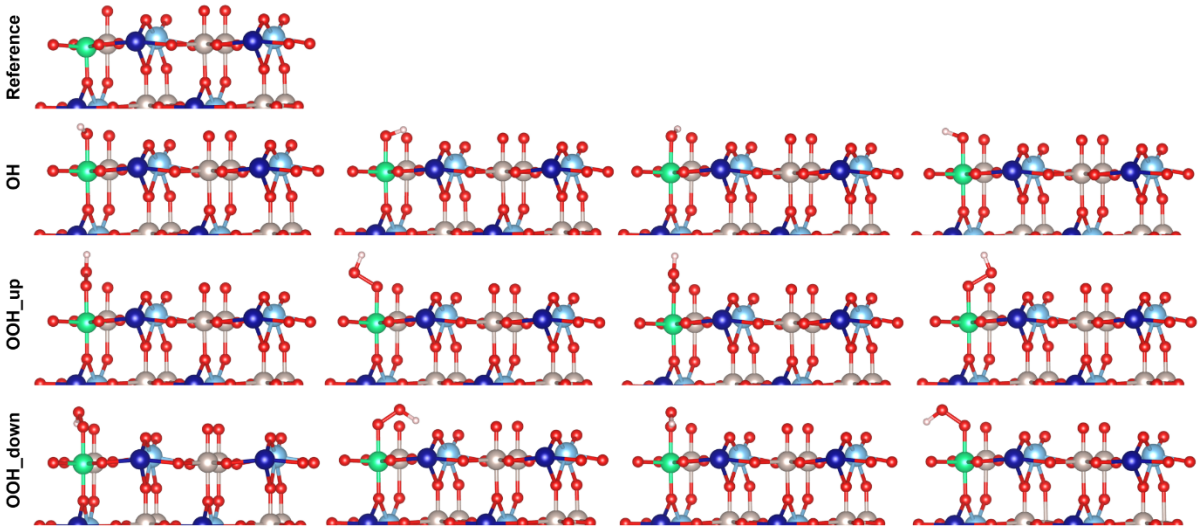


**(b) $RuCrTiO_x$ (101)**

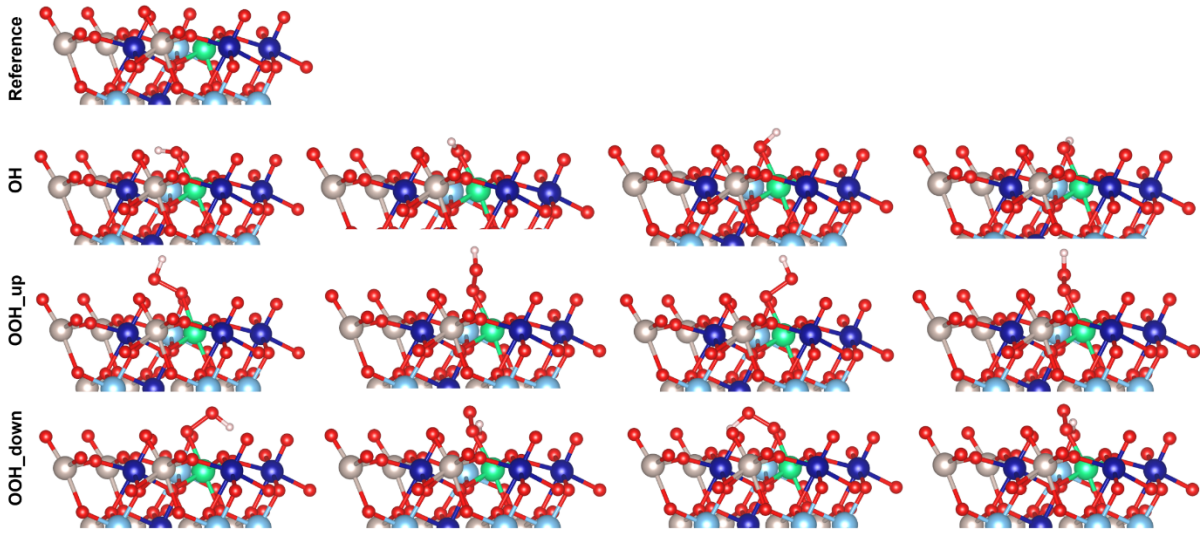


**Figure S26.** $RuCrTiO_x$ OER Intermediates: From Reference to OH, $OOH_{up}$, and $OOH_{down}$ (1-4) rotations. (*) Green color represents the active site on top of the surface.

# S8 Charge density difference and Bader charges Analysis

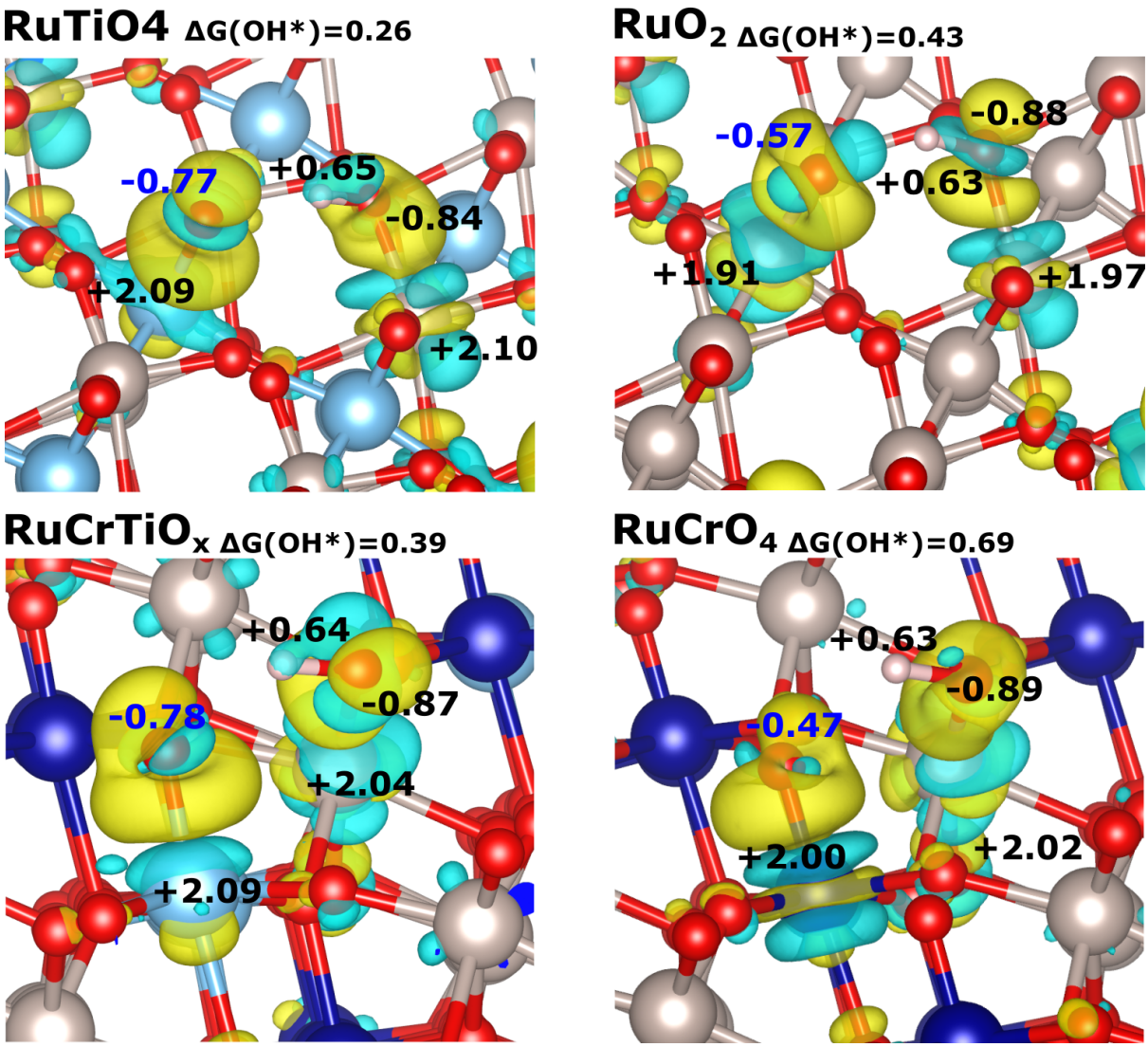


**Figure S27**. Charge density difference with positive (yellow) and negative (light-blue) orbitals, associated ΔG(OH*) and Bader charges for the OH* species at the (101) facet across compositions (RuTiO4, RuCrTiOx, RuO2 and RuCrO4). The M=O* charge located at the O* species are highlighted in blue.

## References


1. Noh, J., Gu, G. H., Kim, S. & Jung, Y. Uncertainty-Quantified Hybrid Machine Learning/Density Functional Theory High Throughput Screening Method for Crystals. *J Chem Inf Model* **60**, 1996–2003 (2020).
2. Akiba, T., Sano, S., Yanase, T., Ohta, T. & Koyama, M. Optuna: A Next-generation Hyperparameter Optimization Framework. *Proceedings of the ACM SIGKDD International Conference on Knowledge Discovery and Data Mining* 2623–2631 (2019) doi:10.1145/3292500.3330701.
3. Kresse, G. & Furthmüller, J. Efficiency of ab-initio total energy calculations for metals and semiconductors using a plane-wave basis set. *Comput Mater Sci* **6**, 15–50 (1996).
4. Kresse, G. & Furthmüller, J. Efficient iterative schemes for *ab initio* total-energy calculations using a plane-wave basis set. *Phys Rev B* **54**, 11169 (1996).
5. Blöchl, P. E. Projector augmented-wave method. *Phys Rev B* **50**, 17953 (1994).
6. Monkhorst, H. J. & Pack, J. D. Special points for Brillouin-zone integrations. *Phys Rev B* **13**, 5188 (1976).
7. Ong, S. P. *et al.* Python Materials Genomics (pymatgen): A robust, open-source python library for materials analysis. *Comput Mater Sci* **68**, 314–319 (2013).
8. Jain, A. *et al.* Commentary: The Materials Project: A materials genome approach to accelerating materials innovation. *APL Mater* **1**, 011002 (2013).
9. Maintz, S., Deringer, V. L., Tchougréeff, A. L. & Dronskowski, R. LOBSTER: A tool to extract chemical bonding from plane-wave based DFT. *J Comput Chem* **37**, 1030–1035 (2016).
10. Sun, W. *et al.* A map of the inorganic ternary metal nitrides. *Nature Materials 2019 18:7* **18**, 732–739 (2019).
11. Ping, Y., Nielsen, R. J. & Goddard, W. A. The reaction mechanism with free energy barriers at constant potentials for the oxygen evolution reaction at the IrO2 (110) surface. *J Am Chem Soc* **139**, 149–155 (2017).
12. Rao, R. R. *et al.* Towards identifying the active sites on RuO2(110) in catalyzing oxygen evolution. *Energy Environ Sci* **10**, 2626–2637 (2017).
13. Rossmeisl, J., Qu, Z. W., Zhu, H., Kroes, G. J. & Nørskov, J. K. Electrolysis of water on oxide surfaces. *Journal of Electroanalytical Chemistry* **607**, 83–89 (2007).
14. Zhang, B. *et al.* Homogeneously dispersed multimetal oxygen-evolving catalysts. *Science (1979)* **352**, 333–337 (2016).

15. Ravel, B. & Newville, M. ATHENA, ARTEMIS, HEPHAESTUS: Data analysis for X-ray absorption spectroscopy using IFEFFIT. *J Synchrotron Radiat* **12**, 537–541 (2005).
16. Kaznatcheev, K. v. *et al.* Soft X-ray spectromicroscopy beamline at the CLS: Commissioning results. *Nucl Instrum Methods Phys Res A* **582**, 96–99 (2007).
17. Sun, T. *et al.* Soft X-ray Ptychography Chemical Imaging of Degradation in a Composite Surface-Reconstructed Li-Rich Cathode. *ACS Nano* **15**, 1475–1485 (2021).
18. Jacobsen, C., Wirick, S., Flynn, G. & Zimba, C. Soft X-ray spectroscopy from image sequences with sub-100 nm spatial resolution. *J Microsc* **197**, 173–184 (2000).